Supplements

Seafloor temperature measurements

The temperature gradients were measured using a 5 m-long temperature-gradient lance with six miniaturized temperature data loggers (MTL). These loggers measured the temperature at a sampling rate of 1 s with an absolute accuracy of approximately 0.1 K (Pfender and Villinger 2002). The relative temperature resolution is 0.001 K. In addition, at six sites a 5 m-long gravity corer with attached MTLs was used. An additional logger at the top of both instruments measured the bottom water temperature as a reference. All measurements were tilt corrected. The derived temperature data were not corrected for sedimentation and terrain effects.

We have measured the thermal conductivity on recovered core material that was sampled at or close to the depth of the measured temperature positions using the KD2 Pro Needle Probe Instrument. For the samples without a thermal-conductivity measurement, i.e. those without cores, we assumed a constant thermal conductivity of 0.7 W/m K. The data were processed using the method published by Hartmann and Villinger (2002). This method determines undisturbed sediment temperatures from the observed temperature decays. Heat flow values were calculated by using Fourier's Law as the product of the temperature gradient and thermal conductivity.

We used Bullard method in which the integrated thermal resistance is plotted as a function of temperature. Usually this relationship is linear. However, transient processes such as high sedimentation rates, seasonal temperature fluctuations, focused advection processes or heat generation may cause non-linear deviations. Fourteen out of the 15 presented heat flow sites show a linear relationship between temperatures as function of integrated thermal resistance. Just one site shows non-linear relation at shallow sediment depth.

We interpret the overall high heat flow values with large lateral variations as a result of hydrothermal fluid movements along narrow pathways. The high

temperature gradient (Supplementary Table DR1) excludes conductive heat transfer. Conductive heat transfer cannot explain either the large lateral heat flow variations on a spatial scale of 100 m. This indicates that there is rigorous hydrothermal venting. All of the SO241-70 sites show advective components. Three out of these four are interpretable as discharge areas (in the northern and central part of the graben), but the Bullard plot of (Site SO241-70P04) shows a downward concave curve at shallow depth, which may be the result of seawater recharge into the crust before it is being heated up.

Geochemistry

Water samples were taken by using a towed SBE9-CTD rosette device equipped with 11 Niskin bottles (a 10 l) and additional HydroC-pCH_4 and -pCO_2, turbidity, and bottom distance sensors (modified after Schmidt et al., 2015). CTD-Stations VCTD09 (and -10) were towed directly above the hydrothermal vent field in variable distance to seafloor (Fig. 3). However, only VCTD09 data is shown in Table S2 as it exhibit notable inorganic variations of hydrothermal tracers in water masses in 5-20 m distance to seafloor. Niskin bottles were closed when temperature, pCO_2 and turbidity suddenly increased indicating hydrothermal plume anomalies. The Niskin bottles were sub-sampled directly after CTD retrieval for inorganic element chemistry, nutrients, partial pressures of dissolved gases and stable and radio-isotope characteristics (Tab. DR2) and water samples were analysed onboard for nutrient concentrations. Sub-samples taken for the analysis of major cations (Na^+, K^+, Li^+, Mg^{2+}, Ca^{2+}, Sr^{2+}, Ba^{2+}) as well as B and Si were measured in the shore-based laboratory at GEOMAR Helmholtz-Centre for Ocean Research by ICP-OES (*http://www.geomar.de/en/research/fb2/fb2-mg/benthic-biogeochemistry/mg-analytik/icp-aes/*). ICP sub-samples were acidified directly after sampling to prevent any precipitation of minerals. The elements Ba, Mn, Si, and Li are enriched compared to seawater values. The concentration ranges between 128 – 1766 nM for Ba, 0.02 to 23.9 µM for Mn, 0.16 – 0.69 mM for Si and 23.1 – 59.2 µM for Li (Table S2). All elements show the strongest anomalies (mostly enrichment) in bottle 12 (VCTD09). Mg shows a slight concentration decrease

compared to seawater. The strongest depletion of Mg (51 mM) was also encountered in bottle 12. TIMS measured $^{87}Sr/^{86}Sr$ ratios normalized on SRM-987 (0.710248) ranges between 0.708906 and almost modern seawater (0.709176) matching 0.709170 (± 1 E-5, typical 2 SEM this session) showing the lowest value in bottle 12 which was sampled closest to the active vent.

We calculated the amount of hydrothermal fluids in the Guaymas Basin bottom water using a simple two-end member mixing model between the seawater and primary hydrothermal fluid which was assumed to be void of Mg. Based on this we calculated the maximum percentage of the hydrothermal fluid in the water samples. The lowest Mg concentration of 51 mM in the water sample of bottle 12 yields a hydrothermal fluid percentage of ~6 %. Based on this we determined the hydrothermal end member composition of the enriched elements in the sampled water column and compared those to the concentrations measured at the southern Guaymas spreading centre by Von Damm et al. (1985).

Hydrothermal end member concentrations for Si and Ba yielded 9.36 mM and 28 µM, respectively and fall well into the end member concentration ranges observed by Von Damm et al. (1985) in the southern Guaymas Basin (Si: 9 - 14 mM; Ba: 7 – 42 µM). Si concentration is at the lower end of the concentration range and might point to a lower hydrothermal temperature or Si precipitation during ascent or after fluid discharge. Hydrothermal end member concentrations calculated for Mn yield 420 µM, which is higher than the concentrations observed in the southern Guaymas hydrothermal fluids, which range between 128 and 236 µM (Von Damm et al., 1985). Von Damm et al. (1985) propose the precipitation of alabandite (MnS) as an explanation for the observed low values. Li, in contrast, shows slightly lower calculated end member concentrations (584 µM) compared to the southern Guaymas fluids, which range between 630 and 1076 µM. These lower values might be explained by a Li sink in the sediments through which the hydrothermal fluids percolate.

Concentrations of dissolved He and Ne (as well as Ar, Kr and Xe) and the $^{3}He/^{4}He$, $^{22}Ne/^{20}Ne$, $^{36}Ar/^{40}Ar$ isotope ratios in water samples taken in copper

tubes were analysed as routine samples in the noble gas laboratory of the Swiss Federal Institute of Technology Zurich (ETHZ) and the Swiss Federal Institute of Aquatic Science and Technology (Eawag). Details on sampling and of the experimental method are given in Beyerle et al. (2000). He and Ne concentrations are covered with an overall standard error of ±2%, the $^{3}He/^{4}He$ ratio has a standard error of 1%.

For the on-board analysis concentrations of dissolved He, Ar, Kr, N_2, O_2, CO_2, and CH_4 during the expedition, we used a portable gas-equilibrium membrane-inlet mass-spectrometric system (GE-MIMS) similar to that described in Mächler et al. (2012). Whereas the original GE-MIMS was designed for gas analysis in continuous high-volume water flows through a large membrane contactor, the GE-MIMS used here was modified to allow analysis of an 8 l water sample taken from a 10 l Niskin sampler within 10 min (Brennwald et. al., 2015, a, b). To allow reliable gas analysis in this limited amount of water, the gas consumption from the membrane contactor into of the MS was reduced to 0.1 ccSTP/min (> 2 ccSTP/min in the original GE-MIMS). This allowed maintaining gas/water solubility equilibrium in miniature membrane contactor modules (two LiquiCel MicroModules operated in parallel) at a total water throughput of 0.5 L/min (> 5 L/min in the original GE-MIMS). The low gas consumption was achieved by replacing the capillary flow resistance followed by a split-flow/aperture gas inlet to the MS vacuum by a new splitless design using a single capillary (9 m long, 0.1 mm inner diameter, Brennwald et al., 2015b). The gas outflow from the capillary is analysed in a quadrupole MS (Stanford Research Systems RGA 200) operated in dynamic mode. As the membrane contactors operate at solubility equilibrium, the partial pressures of the noble gases N_2 and O_2 in the gas phase of the membrane contactors are similar to those in air. The GE-MIMS data for these species were therefore calibrated using ambient air as a reference gas (< 5 % accuracy, 1 σ). The partial pressures of CO_2 and CH_4 are reported as un-calibrated raw data.

In order to determine the variation of excess amounts of the noble gas radon ($^{222}Rn_{(exc.)}$) close to the hydrothermal vent, selected CTD samples were measured

on board by Liquid Scintillation Counting (LSC). Using a portable Hidex Triathler™ system and MaxiLight™ as scintillation cocktail for the measurement of total ^{222}Rn content uncertainties of 15% (SD) are typical for the counting statistics. After more than 3 months storage re-measurements were conducted at GEOMAR to correct for the fraction of total ^{222}Rn potentially provided by the decay of dissolved ^{226}Ra. The analytical procedure followed the approach described by Purkl and Eisenhauer (2004). The maximum sample size was restricted to 1.5 l combined with 20 ml of LSC cocktail, which is close to the maximum extraction efficiency as recently deduced by Schubert et al. (2014). The re-measurements for supported ^{222}Rn contribution did not reveal concentrations above the detection limit of the applied LSC setup. Consequently, a simple, robust, and reliable semi-quantitative measure on the relative enrichment in $^{222}Rn_{(exc.)}$ can be presented in Tab. DR2 in terms of enrichment factors compared to bottle 5. Since bottle 5 shows the lowest ^{222}Rn activity in dpm/L (decay per minute/liter) of the investigated CTD casts it provides the best available approximation to water column background ^{222}Rn activity and was set as reference point (Tab. DR2). The lowest published ^{222}Rn data (0.1 and 0.2 dpm/L) of Santos et al. (2011) for central waters of the Concepcion Bay (West of our study area) and of Prol-Ledesma et al. (2013) for the northern Gulf of California (Wagner and Consag basins, down to zero dpm/100L) may be assumed as typical background values and are similar to the lowest values that we have encountered (bottle 5, 1768 m: 0.17 dpm/L (± 0.1, SD; calibration pending). However, applying the same approach to the sample recovered closest to the vent (bottle 12, 1773 m) yielded the maximum $^{222}Rn_{(exc.)}$ activity of 13.8 dpm/L for our data set. Independent from exact quantitative setup calibrations, this approach provides a robust enrichment factor for $^{222}Rn_{(exc.)}$ in the same order of magnitude as deduced for He in this study (Tab. DR2). However, almost twice as high levels of $^{222}Rn_{(exc.)}$ of 2430 dpm/100L were reported for the hydrothermal impact on the waters of the northern Gulf of California in the Wagner and Consag basins (Prol-Ledema et al., 2013). There they attribute the positive anomalies of ^{222}Rn to a fault system coinciding with the presence of strong flares suggesting hydrothermal circulation in a thick sediment cover and revealing the location of up-flow areas.

Dissolved hydrocarbons (C1-C3) from individual water samples were released onboard by equilibration of 112 ml water samples in a septum-sealed 117 ml headspace vial at room temperature (He-head space, 50 µl $HgCl_2$-solution added). Hydrocarbon composition of the head space gas was determined by using a Thermo Trace gas chromatograph (GC) equipped with flame ionization detector (carrier gas: He 5.0; capillary column: RT Alumina Bond-KCl, column length: 50 m; column diameter: 0.53 µm). Precision of ±1-3% was achieved when measuring standard hydrocarbon mixtures. Molar hydrocarbon concentrations in Table S2 were calculated by applying Henry coefficients according to Mackay and Shiu (2006).

Stable carbon isotope ratios of methane and higher hydrocarbons (C1-C3) from water samples were measured by using continuous flow GC combustion - Isotope Ratio Mass Spectrometry. Hydrocarbons were separated in a Thermo Trace GC (carrier gas: He; packed column: ShinCarbon, 1.5 m). The subsequent conversion of hydrocarbons to carbon dioxide was conducted in a Ni/Pt combustion furnace at 1150°C. The $^{13}C/^{12}C$-ratios of the produced CO_2 were determined by a Thermo MAT253 isotope ratio mass spectrometer. All isotope ratios are reported in the δ-notation with respect to Vienna Pee Dee Belemnite (VPDB, analytical precision 0.5 ‰).

Sedimentation Rates

The wet sediment was weighed, freeze dried at -80°C and reweighed to determine the water content, then ground in a mortar. Radionuclides were then measured as follows. Two HPGe detectors were engaged for ^{210}Pb and ^{226}Ra analysis including GMX-type (ORTEC GMX-120265) and well-type (ORTEC GWL-100230) detectors which interfaced to a digital gamma-ray spectrometer (DSPecPlus™). For the GMX-type detector, absolute counting efficiencies for various photon energies were calibrated using IAEA reference materials 327A, 444 spiked soil, CU-2006-03 spiked soil, RGTh and RGU for sample weight at 100g as a reference, and coupled with an in-house secondary standard for

various masses (from 10 to 250 g) to calibrate the effect of sample mass on the attenuation of γ-rays of various energies. For the well-type detector, the counting efficiencies were calibrated by IAEA-RGTh and RGU from 0.5 to 3.5 g. ^{214}Pb was used as an index of ^{226}Ra (supported ^{210}Pb) whose activity concentration was subtracted from that of the measured total ^{210}Pb to obtain excess ^{210}Pb ($^{210}Pb_{ex}$). The ^{210}Pb and ^{214}Pb activities were quantified based on photon peaks centered at 46.52 and 351.99 keV, respectively. The activities of radionuclides were decay-corrected to the date of sample collection. All radionuclide data were calculated on salt-free dry weight basis. Error bars represent ±1σ around the mean based on counting statistics and standard propagation of errors.

Supplementary references not in the main manuscript

Beyerle, U., Aeschbach-Hertig, W., Imboden, D. M., Baur, H., Graf, T., Kipfer, R. (2000) A mass spectrometric system for the analysis of noble gases and tritium from water samples. Env. Sci. Technol., 34, 2042-2050.

Brennwald, M.S., Rüssel, R., Kipfer, R. (2015a) Recent advances in the on-site analysis and process-based interpretation of dissolved (noble) gases in water bodies. Goldschmidt Abstracts, 386.

Brennwald, M.S., Rüssel, R., Kipfer, R. (2015b) Landing (noble) gas analytics in the field: towards real time insitu gas determination. Goldschmidt Abstracts, 387.

Des Marais, D. J., Stallard, M. L., Nehring, N. L. & Truesdell, A.H. Carbon isotope geochemistry of hydrocarbons in Cerro Prieto geothermal field, Baja California Norte, Mexico. *Chemical Geology* **71**, 159–167, 1988.

Hartmann A, Villinger H (2002) Inversion of marine heat flow measurements by expansion of the temperature decay function. *Geophysical Journal International* 148 (3): 628-636. doi:10.1046/j.1365-246X.2002.01600.x

Lupton, J. E. (1979) Helium-3 in the Guaymas Basin: evidence for injection of mantle volatiles in the Golf of California, *Journal of Geophysical Research* 84: 7464.7452.

Mackay, D. & Shiu, W. Y. A critical review of Henry's law constants for chemicals of environmental interest. *J. Phys. Chem. Ref. Data* **10** (4), 1175–1199 (2006).

Mächler, L., Brennwald, M. S., and Kipfer, R. (2012) Membrane inlet mass spectrometer for the quasi-continuous on-site analysis of dissolved gases in groundwater. *Environmental Science and Technology* 46: 8288-8296.

Padilla y Sánchez, R.J., Domínguez Trejo, I., López Azcárraga, A.G., Mota Nieto, J., Fuentes Menes, A.O., Rosique Naranjo, F., Germán Castelán, E.A., Campos Arriola, S.E., 2013, National Autonomous University of Mexico Tectonic Map of Mexico GIS Project, American Association of Petroleum Geologists GIS Open Files series.

Pfender M, Villinger H (2002) Miniaturized data loggers for deep sea sediment temperature gradient measurements. *Marine Geology* 186: 557-570

Prol-Ledesma R.M., Torres-Vera M.A., Rodolfo-Metalpa R., Ángeles C., Lechuga Deveze C.H., Villanueva-Estrada R.E., Shumilin E. and Robinson C. (2013) High heat flow and ocean acidification at a nascent rift in the northern Gulf of California. *Nature Communications*, DOI: 10.1038/ncomms2390.

Purkl S. and Eisenhauer, A. (2004) Determination of Radium Isotopes and ^{222}Rn in a groundwater affected coastal area of the Baltic Sea and the underlying sub-sea floor aquifer. *Marine Chemistry*, 87 . pp. 137-149.

Santos I., Lechuga-Deveze C., Peterson R.N. and Burnett W.C. (2011) Tracing submarine hydrothermal inputs into a coastal bay in Baja California using radon. *Chemical Geology*, 282, pp. 1-10.

Schmidt, M., Linke, P., Sommer, S., Esser, D. & Cherednichenko, S. Natural CO_2 seeps offshore Panarea – A test site for subsea CO_2 leak detection technology. *Marine Technology Society Journal* **49** (1), 19-30 (2015).

Schubert M., Kopitz J. and Chalupnik S. (2014) Sample volume optimization for radon-in-water detection by liquid scintillation counting. *Journal of Environmental Radioactivity*, 134, pp. 109-113.

Von Damm, K. L., Edmond, J. M., Measures, C. I., Grant, B. (1985) Chemistry of submarine hydrothermal solutions at Guaymas Basin, Gulf of California. *Geochimica Cosmochimica Acta* 49: 2221–2237.

Supplementary figures

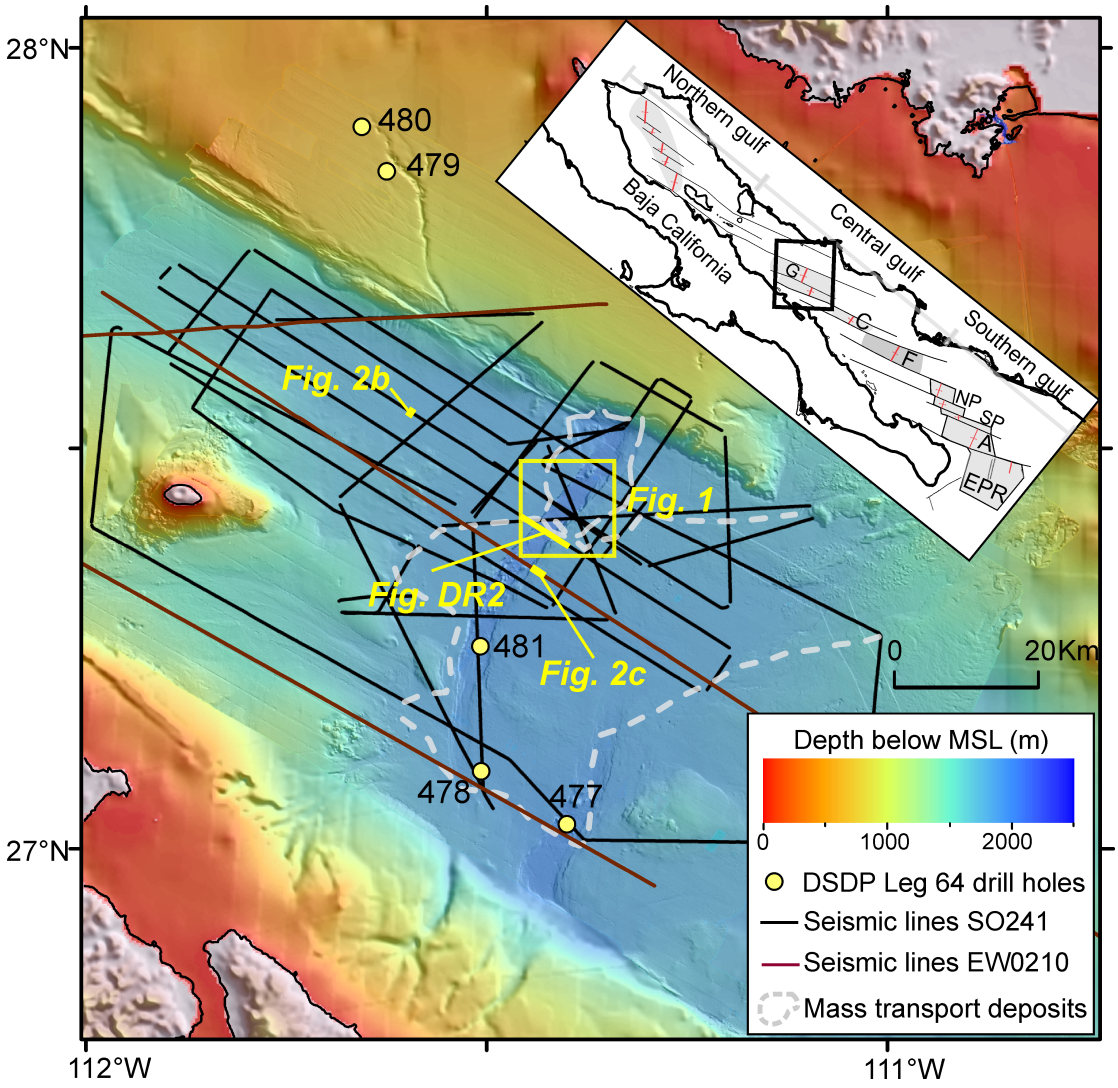

Fig. DR1 – Seismic base map showing the distribution of available 2D seismic data in the Guaymas Basin and major structural elements (after Padilla y Sánchez et al., 2013). Central and Southern gulf spreading centres are labelled, G–Guaymas, C–Carmen, F–Farallon, NP–North Pescadero, SP–South Pescadero, A–Alarcon, EPR–East Pacific Rise.

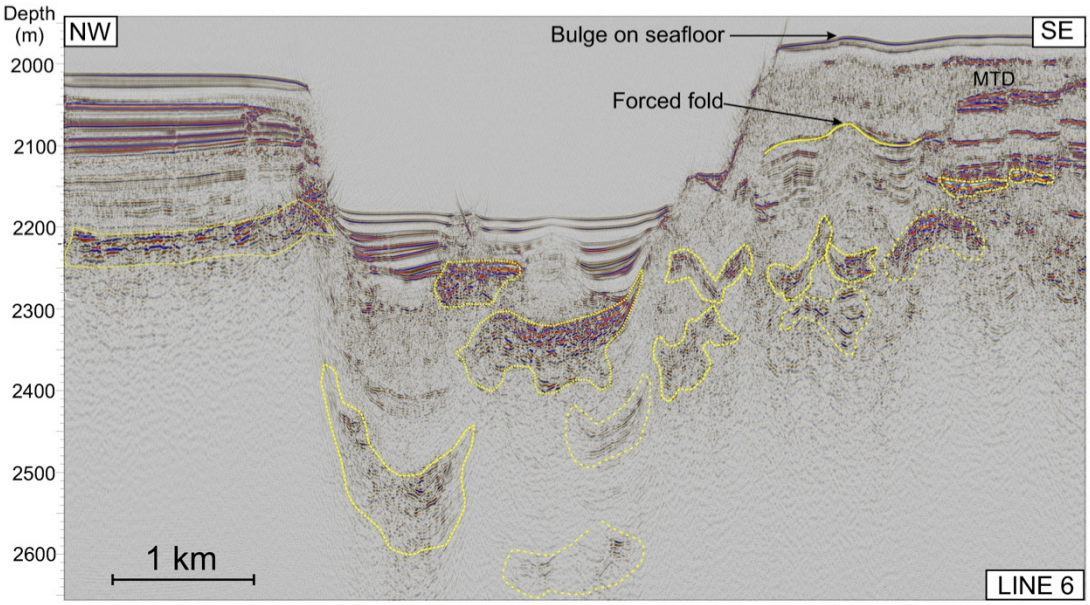

Fig. DR2 – 2D seismic line showing the regional mass transport deposit (MTD) and interpreted sill intrusions (yellow polygons).

Fig. DR3 – Photograph of a massive sulfide sample collected on the southern summit of the mound structure.

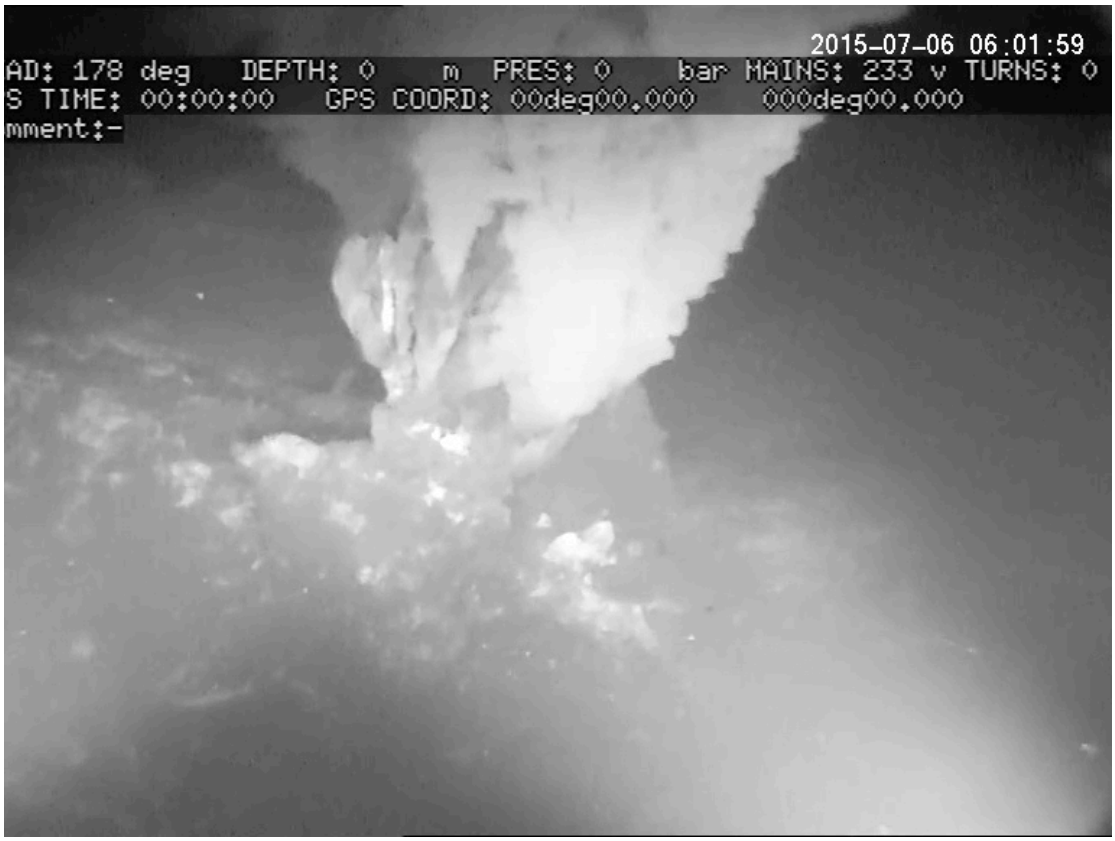

Fig. DR4 – Video still of the easternmost of the seven active vents at top of the mound structure. The vent chimney is approximately 1 m high and 0.5 m across. At least one of the other chimneys is more than 2 m high.

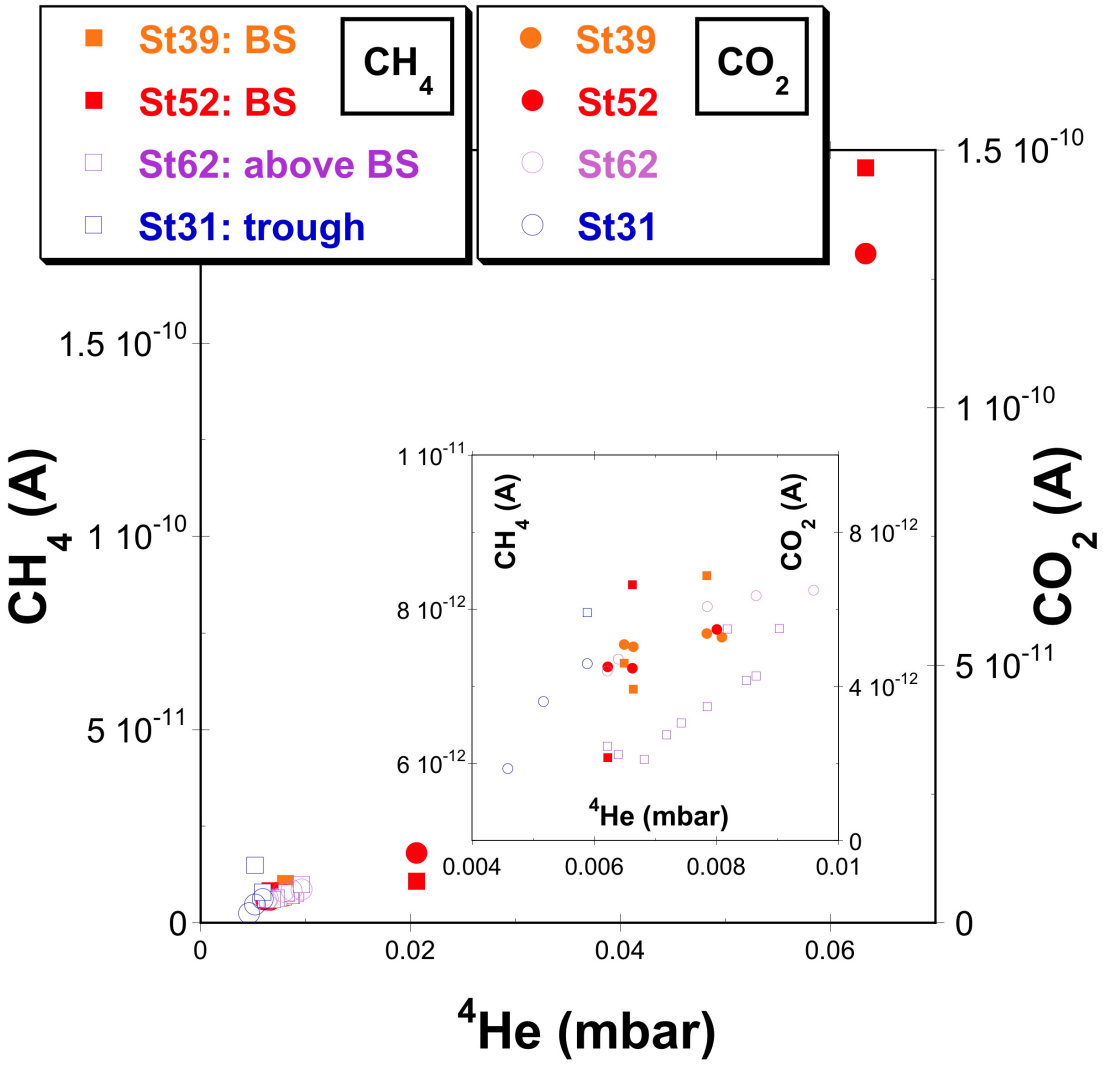

Fig. DR5 - MIMS-determination of dissolved $^{(4)}$He, CH_4 and CO_2 partial pressures (mbar) measured at, above and in the vicinity of the hydrothermal vent site (Stxy: station number xy, BS: 'Black Smoker - within the hydrothermal field (stations: 39, 52)', above BS: 'free water column above vent sites (station 62)', trough: samples in the deep trough of the northern Guaymas Basin (station 31)). The partial pressures of CO_2 and CH_4 are reported as un-calibrated raw MIMS detector signals.

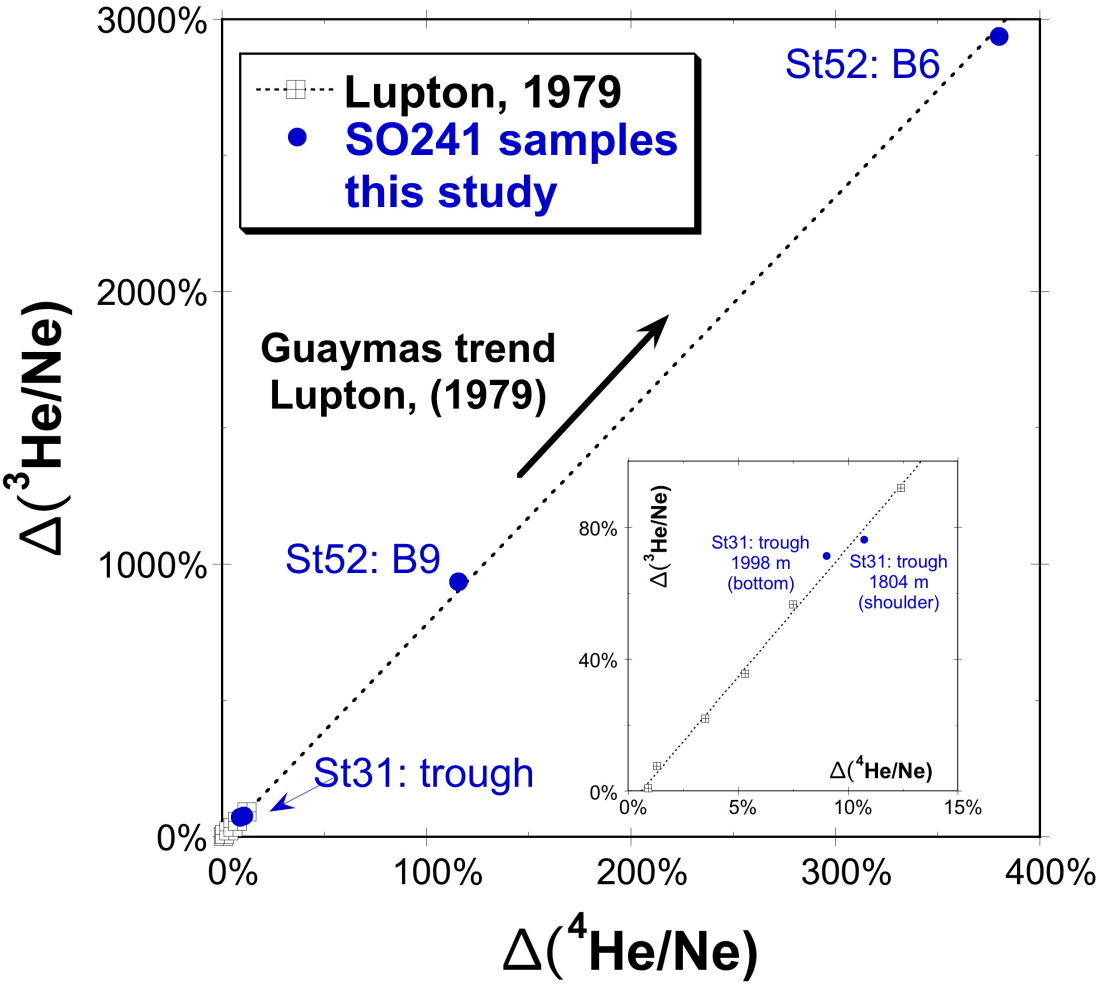

Fig. DR6 - Dissolved He and Ne concentrations measured at the hydrothermal vent site in comparison to earlier noble gas measurements in the southern part of the Guaymas Basin (Lupton, 1979). The samples from the vent site fall on the line defined by the earlier measurements from the southern Guaymas Basin and thus carry isotopic light He ($^3He/^4He$: $10.8 \cdot 10^{-6}$, Lupton, 1979) from the same general MORM source. For comparison noble gas (isotope) concentrations are reported and normalized as in Lupton, 1979:

$$\Delta\left(\frac{^{i}He}{Ne}\right)=\left(\frac{^{i}He_m}{Ne_m}\times\frac{He_{ASW}}{Ne_{ASW}}-1\right)\times 100\ \%$$

where X_m depicts the measured concentration of X, and X_{ASW} is the expected atmospheric equilibrium concentration (atmospheric saturated water: ASW) for the given physical condition of the water. As $^{i}He_{ASW}$ and Ne_{ASW} only barely change

with varying temperature and salinity the $Ne_{ASW}/{}^{i}He_{ASW}$ ratio is virtually independent of the actual physical condition of the water. Stxy: 'station number, 'Bz': bottle number. Station 52: Black Smoker site, Station 31: open water column of the trough.

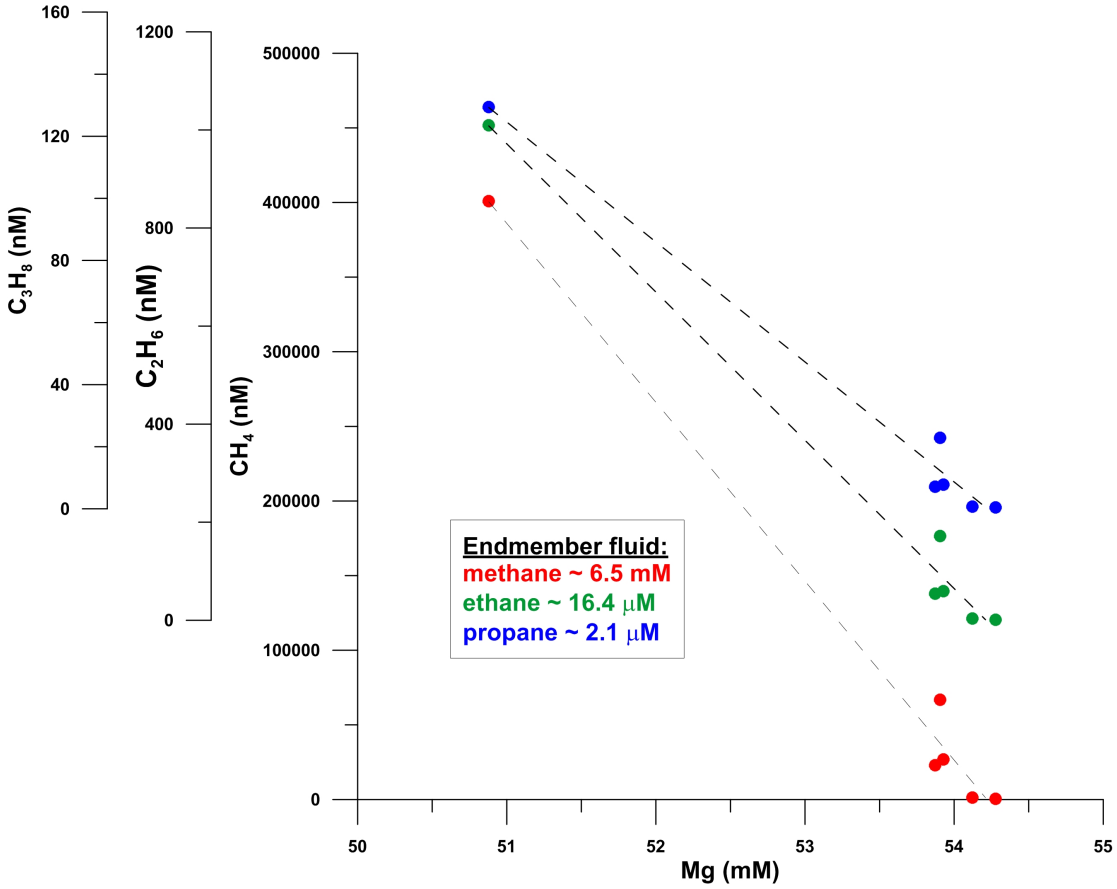

Fig. DR7 - Hydrocarbon end member concentrations (methane, ethane, propane) calculated for hydrothermal fluids venting at the smoker area.

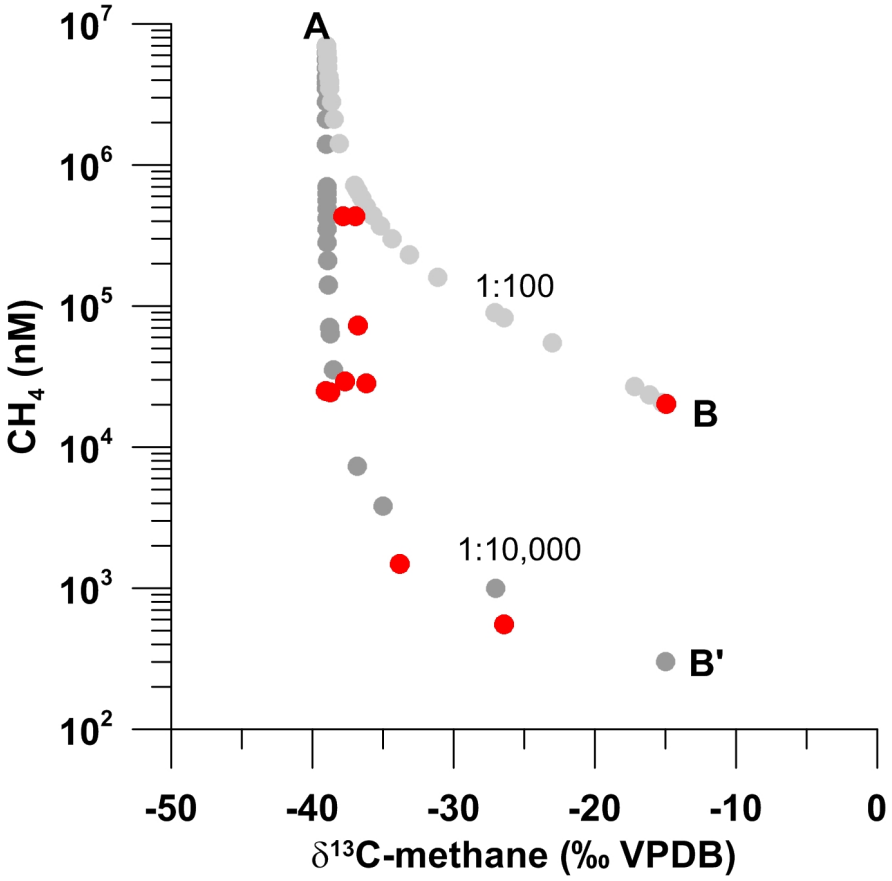

Fig. DR8 - Dissolved methane concentration and carbon isotope data (red dots) determined in bottom water samples from the smoker area. Grey dots indicate mixing curves of a hydrothermal end member methane A (δ^{13}C =-39 ‰, 7nM) with admixture of a second methane-containing fluid B and B' (δ^{13}C =-15 ‰), respectively, at variable dilution factors of 1:100 and 1:10,000 compared to fluid A.

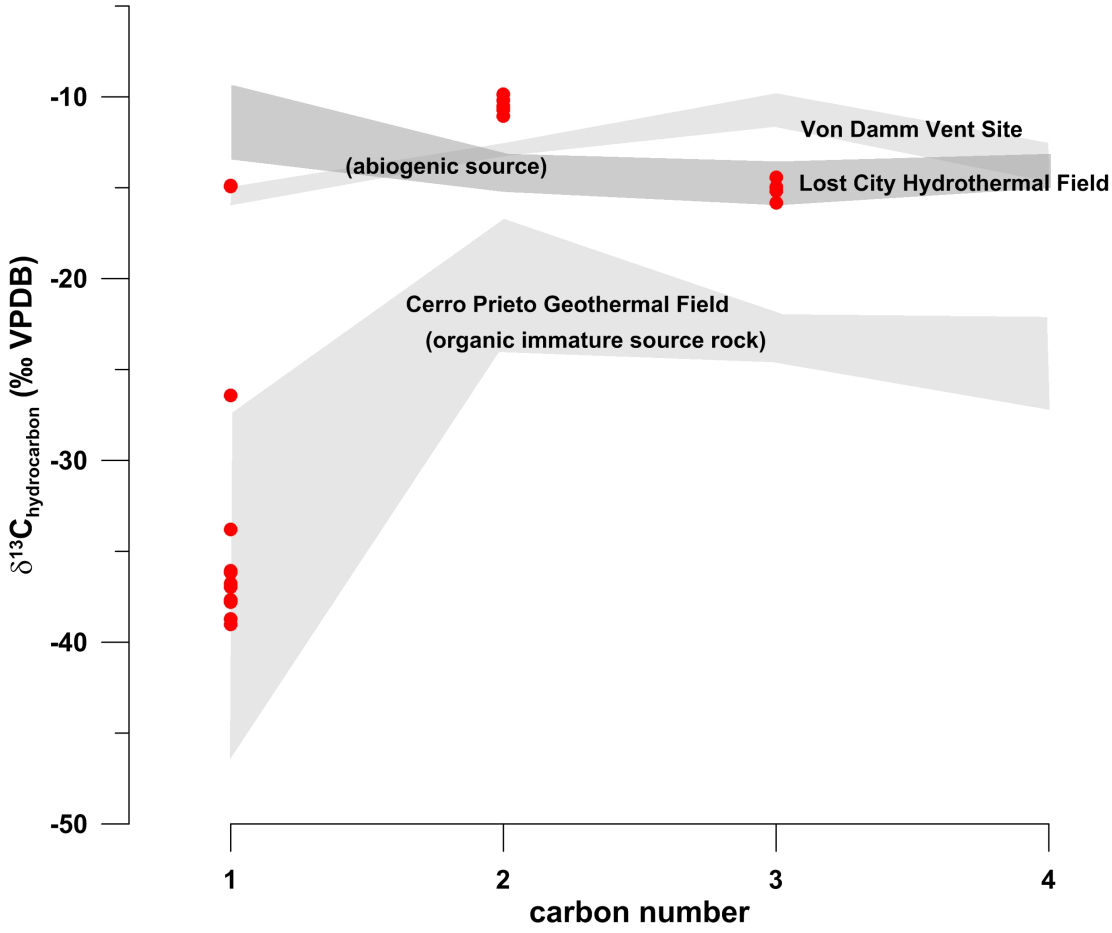

Fig. DR9 - Stable carbon isotope composition of hydrocarbons dissolved in venting hydrothermal fluids (red dots) indicate both hydrocarbons derived from organic matter degradation influenced by volcanic heat intrusion (e.g. Cerro Prieto volcanic complex; Des Marais, 1988), and abiogenic hydrocarbon formation (e.g. Lost City HF, Proskurowski et al., 2008; Von Damm Vent, McDermott et al., 2015).

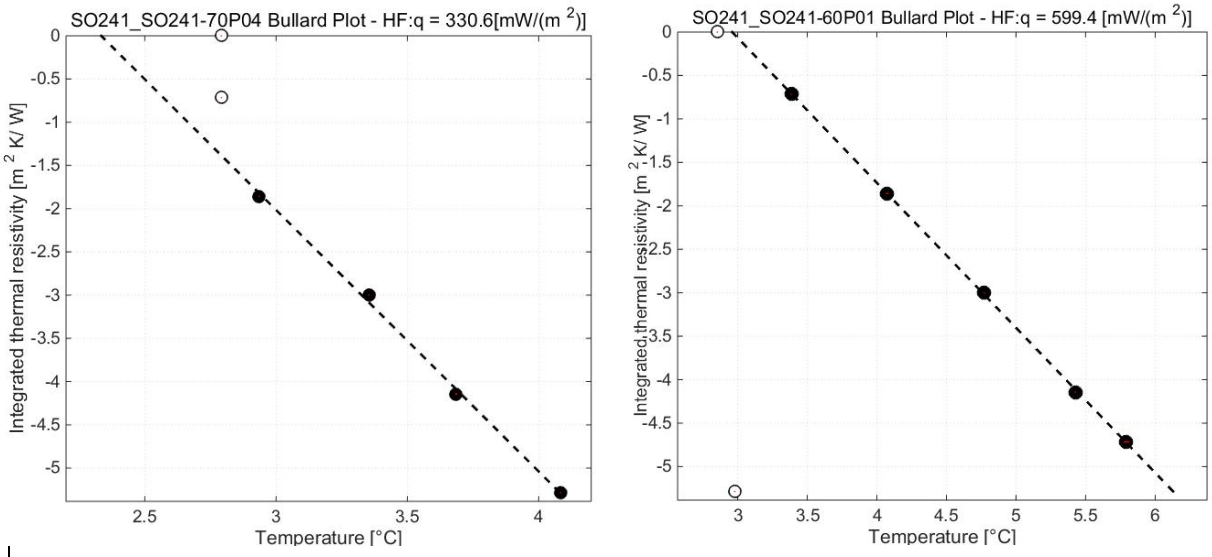

Fig. DR10 - Calculated heat flow for Site SO241-70P04 (top) and SO241-60P01 (bottom) using the Bullard Plot method. Black dots represent sensors used to calculate the heat flow whereas unfilled dots represent the sensor positions, which were not used for any calculations because they were affected by surface artifacts such as incomplete penetration of the lance.

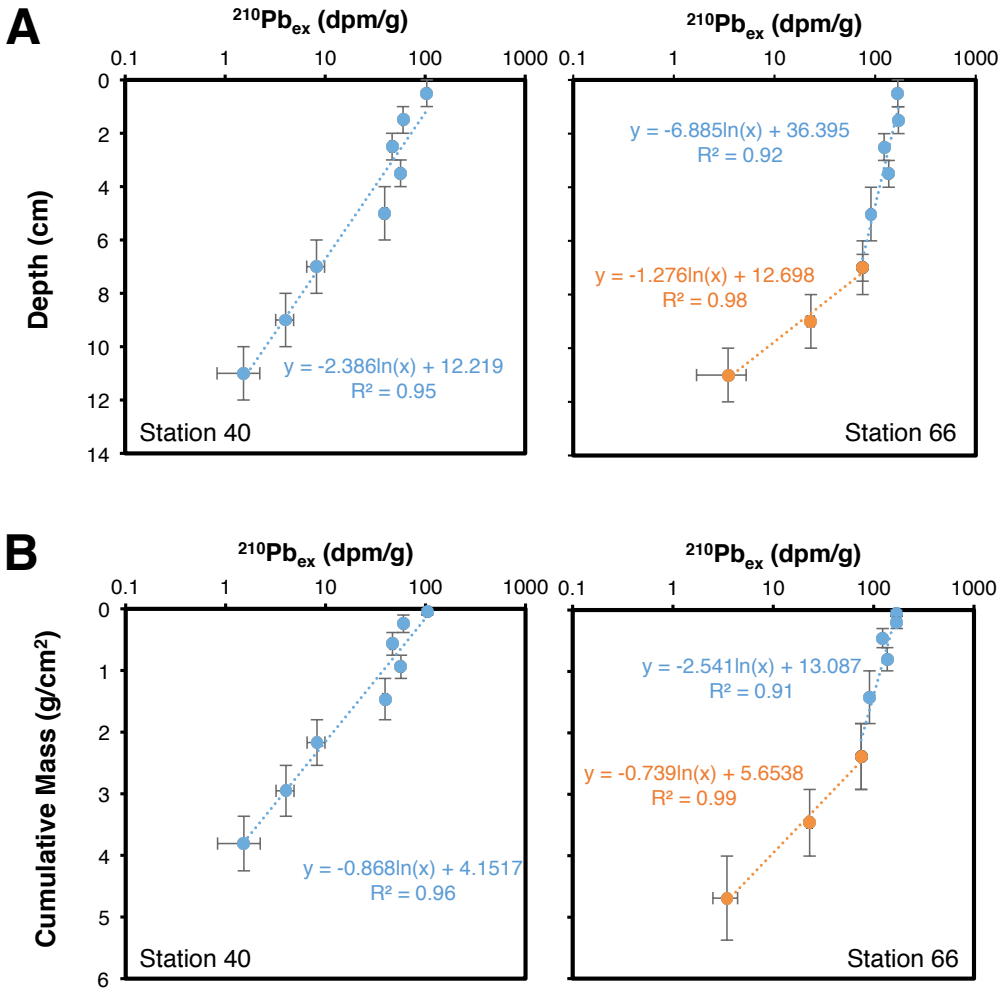

Fig. DR11 – $^{210}Pb_{ex}$ values plotted versus (A) sediment depth and (B) cumulative mass at Stations 40 and 66. Lines and equations represent linear-best fit functions and their data fit (R^2). Station 40 has a good linear fit from the surface to the deepest layers sampled, indicating a relatively steady sedimentation rate over the sampling interval. By contrast, Station 66 has two best-fit lines, one to match samples from the top 6 cm (cyan), and a second one to match samples from 6-12 cm (orange). Samples from the top 6 cm at Station 66 show an only minor decrease in $^{210}Pb_{ex}$, presumably due to vertical sediment mixing by macrofauna. The samples from 6-12 cm at Station 66 show a stronger $^{210}Pb_{ex}$ decrease with depth that more likely reflect the sedimentation rate of the site and were thus used for calculations of sedimentation rates. While the profiles of $^{210}Pb_{ex}$ show good agreement independent of the y-axis units at Station 40, there is a considerable difference between $^{210}Pb_{ex}$ profiles at Station 66 depending on whether sediment depth or cumulative mass are used as y-axis units. This

discrepancy is likely an artefact of core compaction during sediment sampling. We consider $^{210}Pb_{ex}$ relationships with cumulative mass, which correct for compaction effects during coring, to be more reliable (especially at Station 66), and thus report sedimentation rates that have been corrected for cumulative mass in this article.

Supplementary Tables

Table DR1 - Heat flow measurements carried out during SO241

Station	Penetration	Latitude	Longitude	Water Depth [m]	Temp. Gradient [K/m]	k [W/mK]	Heat flow [mW/m²]
SO241-51	Pen 01	27° 24.472'	111° 23.377'	1840	11.441	0.739	8069.3
SO241-58	Pen 01	27° 24.487'	111° 23.377'	1837	9.857	0.720	6508.7
SO241-60a	Pen 01	27° 24.623'	111° 23.626'	1834	0.856	0.7 *	599.4
	Pen 02	27° 24.554'	111° 23.512'	1840	2.789	0.7 *	1952.6
	Pen 03	27° 24.273'	111° 23.396'	1840	4.581	0.7 *	3206.1
	Pen 04	27° 24.408'	111° 23.288'	1849	2.039	0.7 *	1427.0
	Pen 05	27° 24.341'	111° 23.177'	1852	1.014	0.7 *	709.6
	Pen 06	27° 24.265'	111° 23.082'	1844	0.737	0.7 *	516.1
	Pen 07	27° 24.193'	111° 22.956'	1834	0.827	0.7 *	578.7
SO241-60b	Pen 01	27° 24.605'	111° 23.317'	1837	0.391	0.7 *	274.0
	Pen 02	27° 24.552'	111° 23.347'	1834	3.451	0.7 *	2415.4
	Pen 04	27° 24.543'	111° 23.351'	1837	15.479	0.7 *	10835.0
SO241-70	Pen01	27° 25.802'	111° 25.486'	1870	0.375	0.7 *	262.2
	Pen02	27° 25.460'	111° 24.946'	2019	0.483	0.7 *	338.1
	Pen03	27° 25.955'	111° 24.493'	2046	0.432	0.7 *	302.6
	Pen 04	27° 24.837'	111° 23.951	2025	0.457	0.7 *	319.7

Thermal conductivities k with an asterix (*) are assumed.

Table DR2 - Geochemical data of the water column sampled above the black smoker

Bottle	Latitude	Longitude	Depth	Temperature	Salinity	Methane (C1)	Ethane (C2)	Propane (C3)	δ^{13}C-C1	δ^{13}C-C2	δ^{13}C-C3	$^{222}Rn_{(exc.)}$[a]	Mn	Mg	Sr	$^{87}Sr/^{86}Sr$	Si	Ba	Li
	N	W	(m)	(°C)	(‰)	(nM)	(nM)	(nM)	(‰ VPDB)	(‰ VPDB)	(‰ VPDB)	enrich. fact.	(µmol/l)	(mmol/l)	(µmol/l)		(mmol/l)	(nmol/l)	(µmol/l)
1	27.41258	-111.3870	1504	3.1	34.60														
2	27.41284	-111.38696	1766	2.9	34.61	1366.1	3.7	0.8	-33.8				0.02	53.0	88.6		0.16	128	23.1
3	27.41288	-111.38696	1767	2.9	34.61							1.7	<d.l.	54.1	88.7	0.709170	0.18	145	24.9
4	27.41204	-111.38732	1768	4.1	34.55	508.2	0.8	0.4	-26.4				0.14	52.8	88.2		0.18	147	23.3
5	27.41204	-111.38732	1768	4.1	34.64							1.0	<d.l.	54.3	89.2	0.709167	0.18	143	24.9
6	27.4121	-111.38732	1768	4.3	34.68	66885.7	171.7	22.9	-36.8	-9.9	-15.8		0.49	52.9	88.4		0.18	451	23.8
8	27.4121	-111.38732	1768	4.4	34.62							16.2	3.79	53.9	89.6	0.709129	0.26	946	29.0
9	27.41212	-111.38734	1772	6.9	34.64	26801.6	59.1	7.8	-37.7	-10.5			1.33	53.9	88.6	0.709156	0.20	410	26.5
						26010.5	57.4	8.2	-36.2										
10	27.41214	-111.3872	1775	17.4	34.96	22987.6	54.2	7.1	-39.0	-11.1		4.5	1.18	53.9	88.9	0.709159	0.20	383	26.3
						22466.2	52.1	6.8	-38.7										
11	27.41214	-111.3872	1775	28.0	34.17	18684.1	42.6	6.1	-14.9	-10.7	-14.4		1.10[b]	52.9[b]	88.3[b]		0.19[b]	353[b]	24.7[b]
									-14.9										
12	27.41212	-111.38718	1773	12.1	34.26	360284.0	849.3	137.4		-10.2	-15.0								
						400801.8	893.0	110.2	-37.0			81.5	23.9	51.0	90.6	0.708906	0.69	1766	59.2
							1009.3	129.4	-37.8										

[a]Enrichment factor of ^{222}Rn relative to the lowest value measured on this CTD station (bottle 5). See text for details.

[b]Inorganic geochemistry values are a mixture of bottle 10 (~20%) and bottle 11 (~80%)

Table DR3: Isotope ratios of He and Ne reported as the percentage deviations of $^{3}He/Ne$ and $^{4}He/Ne$ from the solubility ratios (see Lupton (1979) for details).

Location	Bottle	Latitude	Longitude	$\Delta(^{3}He/Ne)$ [%]	$\Delta(^{4}He/Ne)$ [%]
		N	W		
Black Smoker	6	27.4121	-111.38732	2937	380
Black Smoker	9	27.41212	-111.38734	936	116
Background trough bottom	2	37.30207	-111.52433	71	9
Background trough shoulder	7	37.30207	-111.52433	76	11